Journal Name

Mononuclear Iron(III) Complex with Unusual Temperature Change of Color and Magneto-Structural Properties: Synthesis, Structure, Magnetization, Multi-frequency ESR and DFT Study[†]

Nitish Kumar Garg,[a] Yogesh Goriya,[a] Seetharaman Manojveer,[a] Senada Muratović,[b] Damir Pajić,[c] Mario Cetina,[d] Irina Petreska,[e] Yulia Krupskaya,[f] Vladislav Kataev,[f] Magnus T. Johnson,*[a] Ola F. Wendt*[a] and Dijana Žilić*[b]

From the reaction of 2-hydroxy-6-methylpyridine (L) with iron(II) tetrafluoroborate, a new mononuclear iron(III) octahedral complex $[FeL_6](BF_4)_3$ has been isolated. The color of the complex is reversible changing from red at room temperature to yellow-orange at liquid nitrogen temperature. Magnetization measurements indicate that iron(III) in $[FeL_6](BF_4)_3$ is in a high-spin state $S = 5/2$, from room temperature down to 1.8 K. High-spin ground state of iron(III) is also confirmed by DFT calculation. Although, the spin-crossover of the complex is not observed, X-band and multifrequency high-field/high-frequency electron spin resonance (ESR) spectroscopy show rather uncommon iron(III) spectra at room temperature and unusual temperature change with cooling. Spectral simulations reveal that the $S = 5/2$ ground state mutiplet of the complex can be characterized by the temperature independent axial zero-field spliting parameter of $|D| = +2$ GHz $(0.067$ cm$^{-1})$ while the value of the rhombic parameter E of the order of some tenths MHz increases with lowering the temperature. Single crystal X-ray diffraction (SCXRD) shows that the iron(III) coordination geometry does not change with temperature while supramolecular interactions are temperature dependent, influencing on the iron(III) rhombicity. Additionally, the DFT calculation shows temperature variation of the HOMO-LUMO gap, in agreement with temperature changes of color and ESR-spectra of the iron(III) complex.

1 Introduction

Design of new materials with desired magnetic and other properties is a demanding task in the field of molecular magnetism. Iron complexes have been widely investigated as magnetic materials but also in the context of metallo-proteins.[1–4] Mononuclear high-spin iron complexes, due to numerous transitions between magnetic levels in a single molecule, can also serve as qubits – the basic units in quantum information processing.[5] Both iron(II) and iron(III) complexes can show spin-crossover (SCO) from the high-spin (HS) to low-spin (LS) state and such SCO can be induced by a change of temperature, magnetic field, pressure or by light irradiation.[6–8] SCO of the iron(III) complex can also take place from the intermediate (IS) to HS state.[9] SCO generally modifies the magnetic and electronic structure of the metal ion and the whole complex thereby significantly changes the physical and chemical properties. An interesting phenomenon often related to SCO is thermochromism – the ability to change color upon change in temperature. This phenomenon has been observed in various classes of organic and inorganic compounds[10–12] as well as in iron complexes.[13–16] However, there are also certain iron(III) compounds where thermochromism was not caused by SCO, although such cases are rare.[17,18]

Changing simultaneously the magnetic behavior and color is interesting because of possible applications such as thermal indicators, switches, optical displays, data storage devices among other interesting fields.[14] To understand magnetic and optical properties, it is necessary to describe energy levels of the inves-

[a] Lund University, Department of Chemistry, P.O. Box 124, S-221 00 Lund, Sweden. Email: magnus.johnson@chem.lu.se, ola.wendt@chem.lu.se
[b] Ruđer Bošković Institute, Bijenička cesta 54, 10000 Zagreb, Croatia. Email: dijana.zilic@irb.hr
[c] University of Zagreb, Faculty of Science, Department of Physics, Bijenička cesta 32, 10000 Zagreb, Croatia.
[d] University of Zagreb, Faculty of Textile Technology, Department of Applied Chemistry, Prilaz baruna Filipovića 28a, 10000 Zagreb, Croatia.
[e] Ss. Cyril and Methodius University in Skopje, Faculty of Natural Sciences and Mathematics - Skopje, Institute of Physics, PO Box 162, 1000 Skopje, Macedonia.
[f] Leibniz IFW Dresden, Helmholtzstrasse 20, D-01069 Dresden, Germany.
† Electronic Supplementary Information (ESI) available: Experimental, elemental, UV-Vis, PXRD, additional SCXRD, ESR and DFT materials. See DOI: 00.0000/00000000.

tigated complex. The number and positions of magnetic levels m_S for complexes with spin higher than $S = 1/2$ are described by the axial and rhombic zero-field splitting (ZFS) parameters, D and E, respectively.[5,19] ZFS parameters can be managed by modification of the coordination environment such as changing coordination numbers, ligand fields as well as symmetry.[20–23] The most suitable experimental technique for an accurate determination of the ZFS parameters is multi-frequency electron spin resonance (ESR) spectroscopy operating both at the commercial X-band ($\sim$ 10 GHz) but also at different high frequencies above 100 GHz, the so called high-field/high-frequency ESR (HF-ESR) spectroscopy.[17,23–25] It has an advantage in that in high magnetic fields, the Zeeman term in the spin-Hamiltonian (SH) becomes significantly larger than the ZFS term and therefore, the ZFS parameters can be obtained more precisely.

In this work, a new mononuclear octahedral iron(III) complex $[FeL_6](BF_4)_3$ is presented, where L stands for 2-hydroxy-6-methylpyridine. The complex changes color reversibly from red at room temperature to yellow-orange at low temperature (78 K). The reversible thermochromism was observed in both powder and single crystalline form of the complex. Notably, magnetization measurements show that the complex is in the HS state ($S = 5/2$) from room temperature down to 1.8 K. This observation is also supported by density functional theory (DFT) calculations, which confirm that the ground state of the complex is the HS state. Therefore, the thermochromism of the complex is not caused by SCO. However, regardless the fact that the spin state does not change, the obtained X-band ESR spectra are non-typical for iron(III) ions and additionally show a strong temperature dependence. It is well known that the interpretation of high-spin transition metal spectra is clearly aided by performing experiments at higher frequencies, and therefore multi-frequency HF-ESR spectra were harnessed.[17,26] In addition, for a better understanding of the temperature changes of the complex' color and ESR spectra, we report UV-Vis study and single crystal X-ray diffraction (SCXRD) data at room and low temperature (125 K) along with the corresponding HOMO-LUMO gaps, obtained from DFT.

2 Results and discussion

2.1 Synthesis

The $[FeL_6](BF_4)_3$ was synthesized by reacting $Fe(BF_4)_2 \cdot 6H_2O$ with 6 eq. of 2-hydroxy-6-methylpyridine (L) in dichloromethane. Recrystallization from pentane gave large red crystals with a ca 98% bulk purity. An intriguing feature of the solid material $[FeL_6](BF_4)_3$ is the reversible color of both crystals and powder samples at different temperatures. The color changes from red at room temperature (for both single crystal and powder sample) to orange at 100 K (single crystal), and upon further cooling to yellow at 78 K (powder), Fig. 1.

2.2 UV-Vis spectroscopy

To probe the observed thermochromism in a more quantitative way, variable temperature solid state UV-Vis spectra were recorded. This shows that a sample cooled with liquid nitrogen

has a long featureless tail into the visible whereas the room temperature sample has a strong absorption in the blue-green area of the spectrum (see Fig. S1 in Electronic Supplementary Information (ESI)).
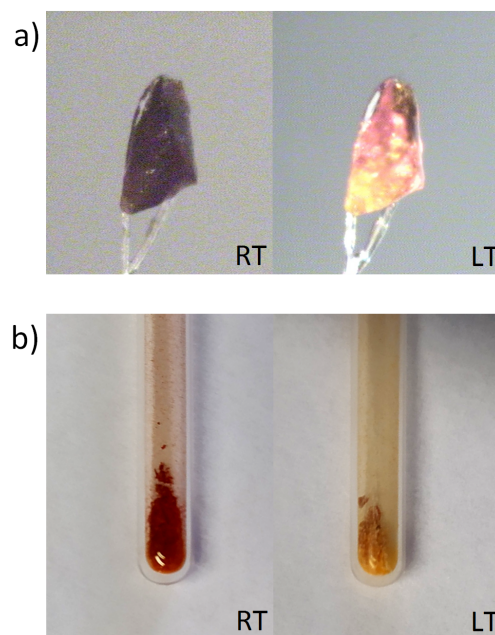

Fig. 1 The color of $[FeL_6](BF_4)_3$ changes with temperature: from red at RT to yellow-orange color at LT: a) single crystal, b) powder sample.

2.3 Single crystal X-ray studies

Data for $[FeL_6](BF_4)_3$(L=2-hydroxy-6-methylpyridine) were collected at room temperature (RT), but also at 125 K (LT) as it is known that structural organization at lower temperature may differ and influence magnetic properties of complexes.[17] In the cations of the complex at LT (Fig. 2) and RT (Fig. S2), the iron(III) ion is octahedrally coordinated by six oxygen atoms from protonated pyridone ligands. Distortion from a regular octahedral geometry is very slight; the *cis* O–Fe–O bond angles are in the range 88.76(11) to 90.51(11)° and 88.8(3) to 91.7(2)° for RT and LT structures, respectively, while *trans* O–Fe–O angles are 178.77(9)° (RT) and 178.0(2)° (LT). Approximately the same geometries of two structures are seen in the overlapping diagram (Fig. S3, ESI). The Fe–O bond lengths and O–Fe–O angles are similar to those observed in closely related structures.[27,28] The conformation of both cations is locked by a weak intramolecular C_{Py}–H···O hydrogen bond (Fig. 2 and Table S1 in ESI).

Hydrogen bonding between the cation and tetrafluoroborate counter anions involves protonated ring nitrogens as donors and fluorine atoms as acceptors. Thus, one N_{Py}–H···F hydrogen bond in $[FeL_6](BF_4)_3$ at RT associates the cation with three tetrafluoroborate counter anions, thus forming a discrete cation/anion assembly (Fig. 3a). A crystal packing diagram along the b axis reveals cation/anion assemblies displaced parallel to the a axis and slightly shifted with respect to each other (Fig. 3b).

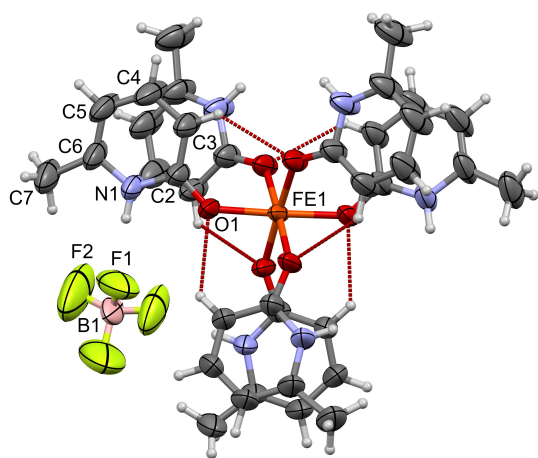In $[FeL_6](BF_4)_3$ at LT, besides N_{Py}–H···F hydrogen bond which forms cation/anion assemblies, one C_{Me}–H···F hydrogen bond is

Fig. 2 Molecular structure of $[FeL_6](BF_4)_3$ recorded at LT, with atom numbering scheme. Displacement ellipsoids for non-hydrogen atoms are drawn at the 50% probability level. Intracation C_{Py}–H⋯O hydrogen bond is indicated by dashed line.

also present (Table S1, ESI). This interaction links neighbouring cation/anion assemblies into two-dimensional layers (Fig. 4a). Each tetrafluoroborate anion is also hydrogen-bonded to two neighbouring cations by two N_{Py}–H⋯F and two C_{Me}–H⋯F hydrogen bonds. The layers are mutually parallel, similarly like the cation/anion assemblies at RT, but much closer so that one C_{Me}–H⋯O hydrogen bond forms a three-dimensional network (Fig. 4b). The distance between planes of oxygen O1 atoms and the closest hydrogen atoms of neighbouring parallel assemblies is 2.496 Å, which is *ca.* 0.54 Å shorter compared to that in $[FeL_6](BF_4)_3$ at RT. That methyl hydrogen atoms are much closer to neighbouring cations compared to those recorded at LT can be seen in Fig. S4 (ESI).

2.4 Powder X-ray diffraction

In order to provide information on the homogeneity of the samples, a powder X-ray diffraction (PXRD) determination was carried out. The Fig. S5 exhibits the X-ray powder patterns of grounded crystals for the iron(III) complex compared to the simulated X-ray powder patterns at room temperature. The patterns are in good agreement indicating that they represent the same phase.

2.5 Magnetization studies

The magnetization properties of $[FeL_6](BF_4)_3$ were investigated using a VSM-SQUID magnetometer. The temperature dependence of the magnetic susceptibility, χ, and its inverse value, $1/\chi$, are shown in Fig. 5. Fitting $1/\chi$ to the Curie-Weiss law in the whole temperature range using

$$\chi = C/(T+\theta) + \chi_0, \tag{1}$$

gives the Weiss parameter $\theta \approx 0$ K ($\theta = 0.069 \pm 0.003$) K, Curie constant $C = (4.08 \pm 0.08)$ erg K/(G^2 mol), $\chi_0 = (2.706 \pm 0.006)10^{-4}$ erg/G^2/mol and confirms the paramagnetic behaviour

of $[FeL_6](BF_4)_3$.[29] From the obtained Curie constant C it is possible to calculate the spin value S of iron(III) ions and gyromagnetic factor g from the relation:

$$g^2 S(S+1) = (3k_B C)/(NN_A\mu_B^2), \tag{2}$$

where $N = 1$ is the number of spins per molecule and other quantities are the well known natural constants. From this relation it follows $S = 5/2$ with $g = 1.93 \pm 0.02$ which is in quite good agreement with the literature.

The magnetic field dependence of the magnetization recorded at the lowest measured temperature 1.8 K is shown in the inset in Fig. 5. The magnetization was recorded changing the magnetic field from 0 to 7 T and back from 7 to 0 T and no magnetic hysteresis was detected. The obtained $M(H)$-curve is in excellent agreement with the Brillouin function for spin $S = 5/2$ shown as a blue curve in the inset in Fig. 5.[29] The value of measured saturation of magnetization is $M_{max} = 4.72\mu_B$, in agreement with the slightly higher theoretical value of $M_{sat} = gS = 5\mu_B$, obtained assuming $g = 2$ and the high-spin value $S = 5/2$ for iron(III) ions at a temperature of 1.8 K[30], as was already expected from the performed Curie-Weiss analysis.

Thus, both $\chi(T)$- and $M(H)$-results indicate that the iron(III) in $[FeL_6](BF_4)_3$ is in the high-spin state $S = 5/2$ in the whole temperature range. Therefore, the spin-crossover of the complex does not take place.

2.6 ESR spectroscopy
2.6.1 X-band spectra

The X-band ESR spectra of the investigated iron(III) complex, obtained at a few selected temperatures, are shown in Fig. 6a) while the spectra with indicated g-factors of the pronounced lines are given in Fig. S6. The spectra were simulated using EasySpin software[31] with the following form of the spin-Hamiltonian for spin $S = 5/2$:

$$\mathbf{H} = g\mu_B \mathbf{B} \cdot \mathbf{S} + D[S_z^2 - S(S+1)/3] + E(S_+^2 + S_-^2)/2 \tag{3}$$

where g is the g-tensor, μ_B is the Bohr magneton, $\mathbf{B}$ is the applied magnetic field while D and E are the previously mentioned axial and rhombic ZFS parameters, respectively.[32] The spectrum at room temperature is simulated with the axial parameter $|D| = 2$ GHz $= 0.067$ cm^{-1} while the rhombic parameter E is taken zero. The unusual temperature change of the spectra was simulated keeping the value of D parameter fixed while increasing with lowering the temperature only the E parameter. The g-value was taken equal to 2 for all simulations. The simulated spectra together with the corresponding D/E ratios are shown in Fig. 6b). The widths of the Lorentzian lines, W_{pp}, used for the simulations are given in Table S3 in ESI. From the simulation of the X-band spectra, it was not possible to determine the sign of the D parameter because the simulation was insensitive to it.

2.6.2 HF-ESR spectra

HF-ESR spectra recorded at the lowest measured temperature of 3 K are shown in Fig. 7. In the same figure, the frequency *vs*
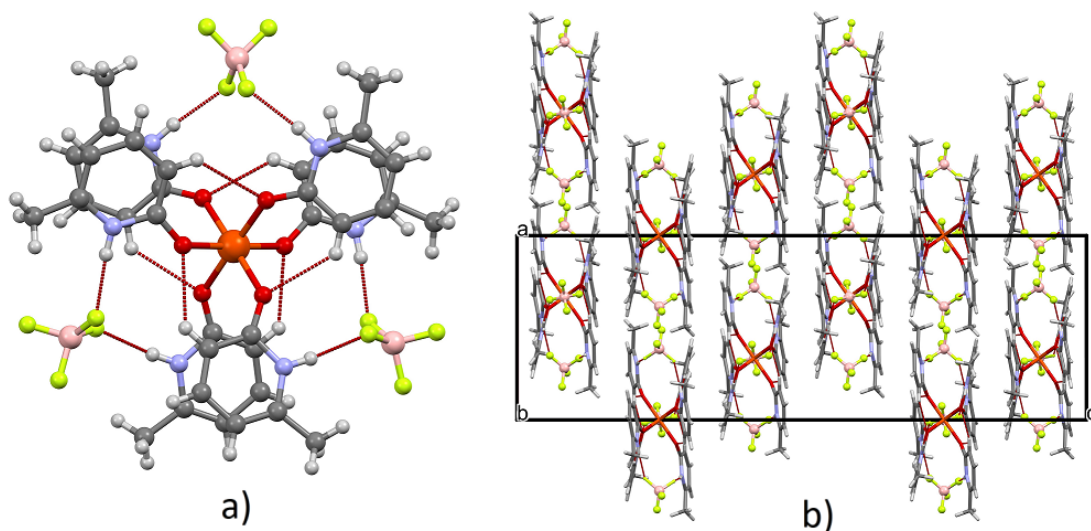
Fig. 3 a) Part of the crystal structure of $[FeL_6](BF_4)_3$ recorded at room temperature, showing discrete cation/anion assembly formed by N–H···F hydrogen bonds. b) Crystal packing diagram of $[FeL_6](BF_4)_3$ at RT, viewed down the b axis, showing parallel arrangements of discrete cation/anion assemblies. Cations are shown by capped-stick representation, while tetrafluoroborate anions are in ball and stick style. Only two major components of disordered fluorine atoms are shown.
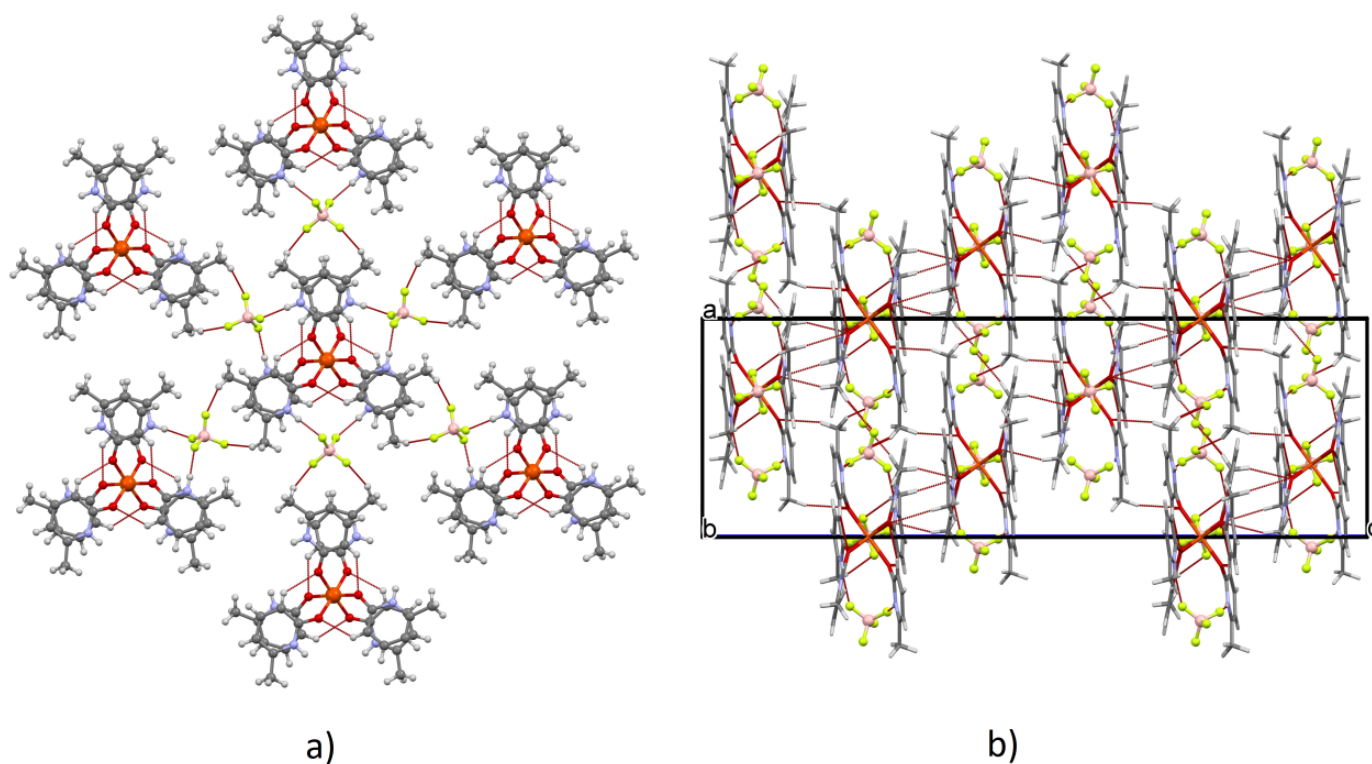

Fig. 4 a) Part of the crystal structure of $[FeL_6](BF_4)_3$ recorded at LT, showing C_{Me}–H···F hydrogen bond that link cation/anion assemblies into two-dimensional layers. b) Crystal packing diagram of $[FeL_6](BF_4)_3$ at LT, viewed down b axis, showing the C_{Me}–H···O hydrogen bond that links the two-dimensional layers into three-dimensional network. Cations are shown by capped-stick representation, while tetrafluoroborate anions are in ball and stick style.

resonant magnetic field diagram is presented. From the prominent spectral points (peak and two shoulders, labeled by arrows in the inset of Fig. 7) three resonance branches (red, black and blue lines) could be obtained. From the slope of these lines, the g-factor values very close to $g = 2$ could be calculated.

The branches are equidistant with the separation corresponding to the y-intercept Δ of the most left (red) line, amounting to $\Delta = 6.873$ GHz ZFS-parameter $|D| = \Delta/4 = 1.720$ GHz.[33] The obtained g- and $|D|$-values are in a good agreement with the values used for the simulations of the X-band spectra (Table S3).
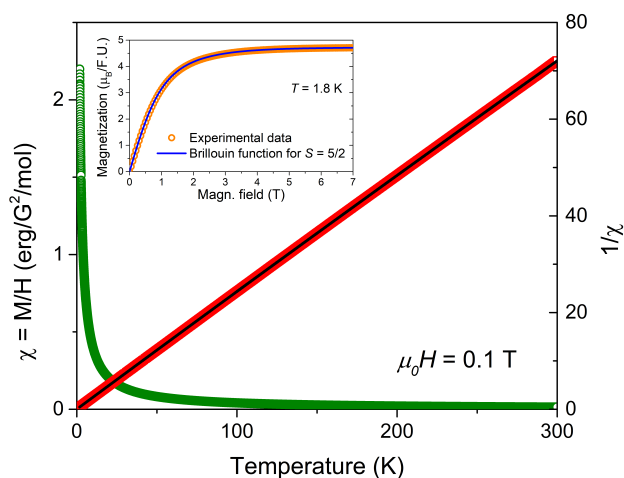
Fig. 5 Temperature dependence of the magnetic susceptibility, $\chi(T)$, (green circles) and the inverse susceptibility, $\chi^{-1}(T)$, (red squares) of the investigated complex in the indicated magnetic field. Black solid line is the fit to the Curie-Weiss law. Inset: Field dependence of magnetization (orange circles) measured at the lowest temperature $T = 1.8$ K, in both directions: 0–7 T and 7–0 T. The blue line is fit of the Brillouin function for $S = 5/2$, multiplied by factor 4.72 ($\approx M_{sat}/\mu_B = gS = 5$).
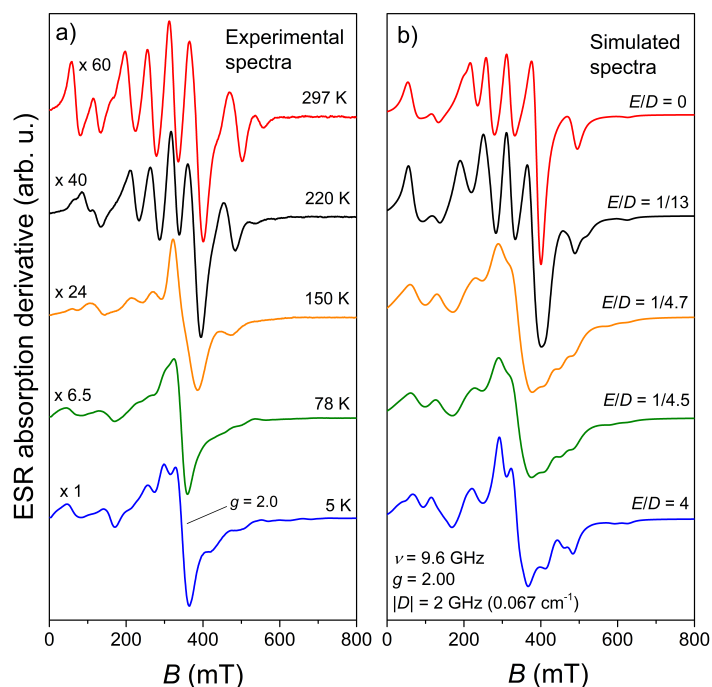

Fig. 6 Temperature dependence of a) experimental and b) simulated X-band ESR spectra of the Fe(III) complex. The intensities of the spectra are multiplied by indicated constant values. The parameters of simulations are given in panel b).

The temperature dependence of the HF-ESR spectra (252 GHz) is presented in Fig. S7 in ESI. Both Figures 7 and S7 show that the HF-ESR spectra do not change significantly with frequency or with temperature. The linewidth of the HF-ESR spectra recorded at 3 K are broader compared to the spectra at higher temperatures 20–150 K, as can be seen in Fig. S7. This might be due to a strong magnetization of the sample causing some inhomogeneous broadening. It should be noticed that the powder sample has been diluted with a non-magnetic material in order to reduce the undesirable effect of the strong magnetization on the spectral shape of the HF-ESR spectra. The parameters used for the simulation of all HF-ESR spectra were the same as those used for the X-band spectra, given in Table S3. The advantage of the HF-ESR analysis compared to the X-band data is that the sign of the axial ZFS parameter D can be determined; while the X-band simulation are non-sensitive to the D-sign, the positive D value enables a better simulation of the HF-ESR spectra.

2.7 DFT study

Motivated by the interesting features that iron based complexes can manifest, including the change of color, we have also carried out DFT calculations to inspect the ground state. A series of DFT optimizations at different levels of theory were done for the doublet, quartet and sextet states of the molecular structure of $[FeL_6](BF_4)_3$, and it was clearly shown that the HS state ($S = 5/2$) is the most stable one. Moreover, the HS and LS states are energetically separated by more than 1 eV (23 kcal/mol), so assuming a Boltzmann distribution, the transition from a ground HS state to an excited LS state is not very likely to be observed, confirming that this complex is not a spin-crossover candidate. Energies of the different states renormalized relative to the energy of HS

state at different levels of theory are summarized in Table S4.

Additionally, DFT calculations were carried out to obtain **g**-tensor values for the HS state, by using GIAO (Gauge-Independent Atomic Orbital) method. Employing B3LYP/6-311++G(2d,2p) level of theory we found the following values: $g_{xx} = 2.224$, $g_{yy} = 2.224$, $g_{zz} = 2.197$. Off-diagonal elements were shown to be negligible. These **g**-tensor values include relativistic mass correction, diamagnetic correction, as well as orbital Zeeman and spin-orbit coupling contribution to the free electron **g**-value. Excluding orbital Zeeman contribution and spin-orbit coupling one finds $g_{xx} = 1.997$, $g_{yy} = 1.997$, $g_{zz} = 1.995$, respectively, which justifies the assumed free-electron g-value in the magnetization study and in simulations of ESR spectra.

Since SCO was not found in the studied complex, we have analyzed molecular orbitals in some more details, given that a possible explanation for the observed color changes with temperature might lie in the temperature effects on the molecular orbitals and more specifically the HOMO-LUMO gap. Several combinations of functionals and basis sets were used to carry out single point DFT calculations on the experimentally determined geometry at two different temperatures, 125 K and 295 K, respectively. Conventionally, when unpaired electrons are present, the highest singly occupied molecular orbital (SOMO) is referred to as the HOMO. In order to be precise, we emphasize here that the studied HOMO-LUMO gap is actually a SOMO-LUMO gap and it is calculated by taking the energy difference between the highest singly occupied molecular orbital and the lowest unoccupied molecular orbital. All DFT calculations were done by using Gaussian series of programming packages. [34]
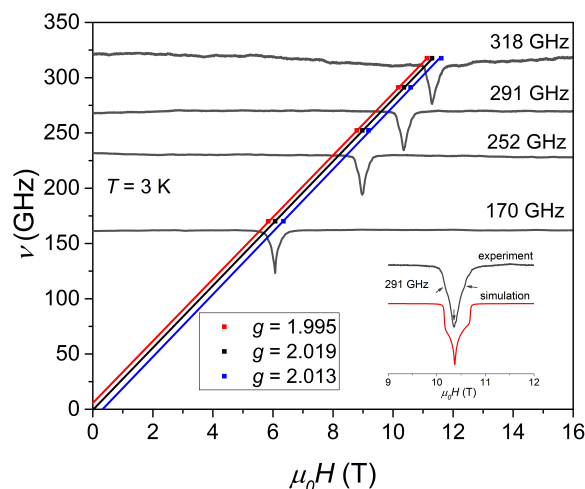
Fig. 7 Frequency *vs* resonance field dependence of the prominent spectral points presented together with corresponding spectra of Fe(III)-complex, measured at different frequencies at $T = 3$ K. Inset shows simulated spectrum at $\nu =$ 291 GHz. Three arrows indicate prominent spectral points (peak and two shoulders) taken in the analysis.

The energy level diagram together with the visualization of the studied orbitals is given in Fig. 8. Also, the neighbouring frontier orbitals are given in Fig. S8 while energy eigenvalues for several frontier molecular orbitals at both temperatures are tabulated in Table S5. Our results show that the HOMO-LUMO gap decreases with increasing temperature. The decrease of the HOMO-LUMO gap with temperature is in qualitative agreement with the experimentally observed UV-Vis spectrum shown in Fig. S1 which shows an absorption peak in the green part of the spectrum at RT, hence the sample appears as red. At lower temperatures (100–150 K) a tail is found in the visible part of the spectra, starting from blue-green part of the spectrum. This means that in the visible part of the spectrum higher wavelengths are absorbed at RT in comparison to LT, which corresponds to the calculated decrease in the HOMO-LUMO gap. One can note that the RT HOMO-LUMO gap corresponds to an absorbance at ca 450 nm which is in good agreement with the recorded experimental UV-Vis solid state spectrum.

Further analysis of the molecular orbitals obtained from DFT calculations shows that this is mainly due to a shift of the LUMO orbital which lies around 0.18 eV lower at RT compared to LT, while the HOMO orbital lies around 0.03 eV higher. A careful observation of the probability density distribution from the visualized orbitals suggests also changes in the molecular orbital localization on the ligands, which is more pronounced in the LUMO orbital (Fig. 8, upper panels). A similar trend is seen in neighbouring LUMOs. According to X-ray structural studies, the distances between methyl hydrogen atoms to neighbouring cations decrease when the sample is cooled down (Figs. 2 and 3). This decrease in the cation/anion distances causes redistribution of the electron probability density on the ligands, most likely via electrostatic interactions, which in turn gives rise to charge transfer (CT) bands in the UV-Vis spectra, as well. It should also be noted here

that contribution of d-d transitions to UV-Vis spectra of the studied complex is expected to be negligible due to selection rules. Consequently, optical transitions are due to ligand-to-metal CT (LMCT), ligand-to-ligand CT (LLCT) and/or metal-to-ligand CT (MLCT).[35] Emergence of CT bands in the UV-Vis spectra is typical for octahedral iron(III) complexes.[36–38] At room temperatures, the LUMO orbital, which according to Fig. 8 is mostly ligand in character, has a lower energy, that might facilitate MLCT (the peak around 450 nm in UV-Vis spectrum at RT) or LLCT. Therefore, electrons from iron-localized molecular orbitals may be excited to molecular orbitals of the π-acceptor ligands via metal-to-ligand charge transfer processes. One can note that the d-orbital contribution to the HOMOs is in the order of 30% and the transition observed will probably have a substantial LLCT character. Any LMCT character is, on the other hand, probably negligible since none of the LUMOs have any significant metal character. The percentages of d-orbital participation in HOMO and LUMO, as well as in the nearest neighbors, at both temperatures, are given in Table S6. One can furthermore note that the LUMO is substantially more delocalized at low temperature compared to room temperature; this could effect the intensity of the observed bands but given the semiquantitative agreement between experiment and calculated HOMO-LUMO we favour the explanation based on a LUMO shift in the solid state.

Additionally, along with the calculations of the molecular orbitals for the neutral molecular moiety $[FeL_6](BF_4)_3$, we have separately analyzed the orbitals for the cation (Fig. S9). Our findings confirm that the changes of molecular orbitals with temperature are due to the effects on cation/anion interactions. Namely, as it can be seen from the visualization of frontier molecular orbitals (Fig. S9) in the cationic structure there is an insignificant temperature change in the electron probability density distribution in the HOMO and LUMO orbitals, as well as in the HOMO-LUMO gap, in comparison to the neutral one.
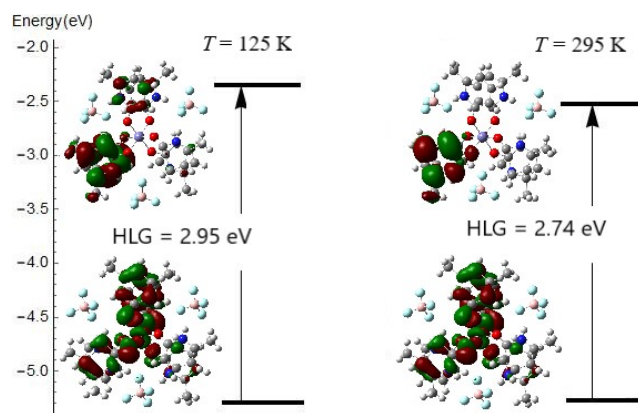

Fig. 8 HOMO-LUMO gap and visualization of HOMO (lower panels) and LUMO (upper panels) orbitals of $[FeL_6](BF_4)_3$ molecular structure at two different temperatures. Presented results are obtained at pbe/6-31g(d,p) level of theory.

3 Discussion

The complexity of the X-band ESR spectra (Fig. 6) is due to a significant axial ZFS parameter D which is comparable with the

energy of the microwave quantum at X-band frequencies. In this situation the states of the three spin doublets of the $S = 5/2$ multiplet of the iron(III) ion are mixed giving rise to many "forbidden" transitions.[39–41] Indeed, as we have shown in the HF-ESR experiment, increasing the energy of the microwave quantum by at least one order of magnitude drastically simplifies the spectra and enable an accurate determination of the parameters of the spin-Hamiltonian (3). Similar rather uncommon ESR behaviour of the $[Fe(DMSO)_6](NO_3)_3$ complex with the axial ZFS parameter $D \approx 0.2$ cm^{-1} was described by Solano-Peralta and co-authors.[17] They also reported a change of the complex color from yellow-orange at RT to pale yellow at 77 K as well as a temperature dependence of the rhombicity E/D due to hydrogen bonding network changing. It is interesting to note that the approximately 3 times larger D-value ($D \approx 0.2$ cm^{-1} compared to our $D \approx 0.067$ cm^{-1}) results in totally different X-band spectra. These two examples show that ESR spectroscopy is extremely sensitive to a change of the ZFS parameters in the $|2D| \approx 10$ GHz regime. Furthermore, these two complexes are also good examples for how using only a standard magnetization characterization technique such as SQUID magnetometry one can completely miss interesting temperature changes of the magnetic properties.

The revealed temperature change of the rhombic parameter E is likely to be related with the structural changes. Single crystal X-ray diffraction recorded at RT and LT shows that the almost ideal octahedral coordination of the iron(III) ion does not change with temperature as can be seen in the overlapping diagram (Fig. S3, ESI). However, this study clearly demonstrates that supramolecular interactions due to hydrogen bonds networks are changing with temperature (Figs. 3 and 4). These structural changes are furthermore manifested in the distribution of frontier molecular orbitals obtained from DFT calculations and in the experimentally observed UV-Vis spectra. As it was analyzed in the previous section, the temperature effects on cation/anion interactions affect charge transfer bands via electron probability density redistribution. This in turn lowers the energy value of the ligand based LUMO orbital, facilitating MLCT and/or LLCT at room temperatures. The negligible change of the cation geometry observed in X-ray crystallography is also in favour of this explanation, as well as the small effect on the HOMO-LUMO when counteranions were excluded in the DFT calculations. Moreover, association of the cations with three tetraflouroborate anions via hydrogen bonds, that enables formation of cation/anion assemblies, and linked via additional hydrogen bond between the layers at LT is evident from single crystal X-ray studies.

4   Conclusion

A new mononuclear iron(III) octahedral complex $[FeL_6](BF_4)_3$ has been synthesized and characterized by elemental analysis, SCXRD and PXRD. Magnetization measurements show that the complex is in its high-spin state $S = 5/2$ from room temperature down to 1.8 K i.e. no spin-crossover takes place. However, the compound changes color from red at room temperature to yellow-orange at liquid-nitrogen temperature, a phenomenon that motivated a closer look into the $[FeL_6](BF_4)_3$ properties. SCXRD at liquid-nitrogen temperature, the temperature-dependent X-band

and HF-ESR spectroscopy and spectral simulations, together with DFT calculation and UV-Vis spectra, provided insights into interesting structural, optical and magnetic temperature behaviour of the complex. Overall, we conclude that thermal fluctuations of intermolecular interactions through hydrogen bonds affect molecular orbital energies, and thereby the optical and ESR spectra of the investigated iron(III) complex giving rise to a rare phenomenon of a non-SCO driven thermochromism in iron(III) compounds.

Notes and references

1 H. Meštrić, R.-A. Eichel, K.-P. Dinse, A. Ozarowski, J. van Tol and L. C. Brunel, *J. Appl. Phys.*, 2004, **96**, 7440–7444.

2 W. R. Hagen, *Dalton Trans.*, 2006, 4415–4434.

3 D. Gatteschi, R. Sessoli and J. Villain, *Molecular Nanomagnets*, Oxford University Press, Oxford, UK, 2006.

4 J. Ferrando-Soria, J. Vallejo, M. Castellano, J. Martínez-Lillo, E. Pardo, J. Cano, I. Castro, F. Lloret, R. Ruiz-García and M. Julve, *Coord. Chem. Rev.*, 2017, **339**, 17–103.

5 J. M. Zadrozny, S. M. Greer, S. Hill and D. E. Freedman, *Chem. Sci.*, 2016, **7**, 416–423.

6 M. A. Halcrow, *Chem. Soc. Rev.*, 2011, **40**, 4119–4142.

7 M. S. Shongwe, S. H. Al-Rahbi, M. A. Al-Azani, A. A. Al-Muharbi, F. Al-Mjeni, D. Matoga, A. Gismelseed, I. A. Al-Omari, A. Yousif, H. Adams, M. J. Morris and M. Mikuriya, *Dalton Trans.*, 2012, **41**, 2500–2514.

8 S. Xue, Y. Guo, A. Rotaru, H. Muüller-Bunz, G. G. Morgan, E. Trzop, E. Collet, J. Ola´h and Y. Garcia, *Inorg. Chem.*, 2018, **57**, 9880–9891.

9 S. Mossin, B. L. Tran, D. Adhikari, M. Pink, F. W. Heinemann, J. Sutter, R. K. Szilagyi, K. Meyer and D. J. Mindiola, *J. Am. Chem. Soc.*, 2012, **134**, 13651–13661.

10 J.-P. Ma, S.-C. Liu, C.-W. Zhao, X.-M. Zhang, C.-Z. Sun and Y.-B. Dong, *CrystEngComm,*, 2014, **16**, 304–307.

11 V. R. Shayapov, A. N. Usoltsev, S. A. Adonin, M. N. Sokolov, D. G. Samsonenko and V. P. Fedin, *New J. Chem.*, 2019, **43**, 3927–3930.

12 C.-R. Huang, X. Luo, X.-G. Chen, X.-J. Song, Z.-X. Zhang and R.-G. Xiong, *National Science Review*, 2021, **8**, nwaa232.

13 M. Nihei, T. Shiga, Y. Maeda and H. Oshio, *Coord. Chem. Rev.*, 2007, **251**, 2606–2621.

14 P. Gütlich, A. B. Gaspar and Y. Garcia, *Beilstein of Org. Chem.*, 2013, **9**, 342–391.

15 C.-F. Sheu, S.-M. Chen, G.-H. Lee, Y.-H. Liu, Y.-S. Wen, J.-J. Lee, Y.-C. Chuang and Y. Wang, *Eur. J. Inorg. Chem.*, 2013, 894–901.

16 J. Yuan, M.-J. Liu, C.-M. Liu and H.-Z. Kou, *Dalton Trans.*, 2017, **46**, 16562–16569.

17 A. Solano-Peralta, J. P. Saucedo-Vázquez, R. Escudero, H. Höpfl, H. El-Mkami, G. M. Smith and M. E. Sosa-Torres, *Dalton Trans.*, 2009, 1668–1674.

18 Y. Nekoud, D. Mezaoui and N. Cosquer, *J. Mol. Struct.*, 2019, **1192**, 59–67.

19 J. Telser, in *EPR Interactions – Zero-Field Splittings*, American Cancer Society, 2017, pp. 207–234.

20 D. Collison and A. K. Powell, *Inorg. Chem.*, 1990, **29**, 4735–4746.

21 K. K. Andersson and A.-L. Barra, *Spectrochim. Acta A*, 2002, **58**, 1101–1112.

22 Y.-F. Deng, T. Han, Z. Wang, Z. Ouyang, B. Yin, Z. Zheng, J. Krzystek and Y.-Z. Zheng, *Chem. Commun.*, 2015, **51**, 17688–17691.

23 D. Žilić, L. Androš, Y. Krupskaya, V. Kataev and B. Büchner, *Appl. Magn. Reson.*, 2015, **46**, 309–321.

24 C. Golze, A. Alfonsov, R. Klingeler, B. Büchner, V. Kataev, C. Mennerich, H.-H. Klauss, M. Goiran, J.-M. Broto, H. Rakoto, S. Demeshko, G. Leibeling and F. Meyer, *Phys. Rev. B*, 2006, **73**, 224403.

25 L. Androš, M. Jurić, J. Popović, D. Pajić, Y. Krupskaya, V. Kataev, B. Büchner and D. Žilić, *Dalton Trans.*, 2018, **47**, 3992–4000.

26 F. Biaso, C. Duboc, B. Barbara, G. Serratrice, F. Thomas, D. Charapoff and C. Béguin, *Eur. J. Inorg. Chem.*, 2005, **2005**, 467–478.

27 A. J. Blake, R. O. Gould, C. M. Grant, P. E. Y. Milne and R. E. P. Winpenny, *Polyhedron*, 1994, **13**, 187–191.

28 D. M. L. Goodgame, D. J. Williams and R. E. P. Winpenny, *Inorg. Chim. Acta*, 1989, **166**, 159–162.

29 N. A. Spaldin, *Magnetic Materials Fundamentals and Applications*, Cambridge University Press, Cambridge, UK, 2013.

30 S. Blundell, *Magnetism in Condensed Matter*, Oxford University Press, Oxford, UK, 2006.

31 S. Stoll and A. Schweiger, *J. Magn. Reson.*, 2006, **178**, 42–55.

32 S. Stoll, *EasySpin –EPR spectrum simulation*, 2021.

33 A. Abragam and B. Bleaney, *Electron Paramagnetic Resonance of Transition Ions*, Clarendon Press, Oxford, UK, 1970.

34 M. Frisch, G. Trucks, H. Schlegel, G. Scuseria, M. Robb, J. Cheeseman, G. Scalmani, V. Barone, G. Petersson, H. Nakat-suji *et al.*, *Gaussian 16, revision C. 01*, 2016.

35 A. K. Brisdon, *Inorganic spectroscopic methods*, Oxford University Press New York, 1998.

36 C. K. Prier, D. A. Rankic and D. W. MacMillan, *Chemical reviews*, 2013, **113**, 5322–5363.

37 P. Chábera, Y. Liu, O. Prakash, E. Thyrhaug, A. El Nahhas, A. Honarfar, S. Essén, L. A. Fredin, T. C. Harlang, K. S. Kjær *et al.*, *Nature*, 2017, **543**, 695–699.

38 M. Wang, J. England, T. Weyhermülller, S.-L. Kokatam, C. J. Pollock, S. DeBeer, J. Shen, G. P. Yap, K. H. Theopold and K. Wieghardt, *Inorganic chemistry*, 2013, **52**, 4472–4487.

39 F. E. Mabbs and D. Collison, *Electron Paramagnetic Resonances of d Transition Metal and Compounds*, Elsevier, Amsterdam, 1992.

40 N. Shaikh, S. Goswami, X.-Y. Panja, A.and Wang, S. Gao, R. Butcher and P. Banerjee, *Inorg. Chem.*, 2004, **43**, 5908–5918.

41 V. I. Murav'ev, *Russ. J. Coord. Chem.*, 2011, **37**, 861–867.